Proof-of-concept Talbot–Lau x-ray interferometry with a high-intensity, high-repetition-rate, laser-driven K-alpha source

V. Bouffetier, L. Ceurvorst, M. Valdivia, F. Dorchies, S. Hulin, T. Goudal, D. Stutman, A. Casner

applied optics

Proof-of-concept Talbot–Lau x-ray interferometry with a high-intensity, high-repetition-rate, laser-driven K-alpha source

V. Bouffetier,[1,*] L. Ceurvorst,[1] M. P. Valdivia,[2] F. Dorchies,[1] S. Hulin,[1] T. Goudal,[1] D. Stutman,[2] and A. Casner[1]

[1]Université de Bordeaux-CNRS-CEA, Centre Lasers Intenses et Applications (CELIA), UMR 5107, F-33405 Talence, France
[2]Department of Astrophysics and Astronomy, Johns Hopkins University, Baltimore, Maryland 21218, USA
*Corresponding author: victorien.bouffetier@u-bordeaux.fr

Received 16 June 2020; revised 4 August 2020; accepted 17 August 2020; posted 20 August 2020 (Doc. ID 398839); published 17 September 2020

Talbot–Lau x-ray interferometry is a grating-based phase-contrast technique, which enables measurement of refractive index changes in matter with micrometric spatial resolution. The technique has been established using a variety of hard x-ray sources, including synchrotron, free-electron lasers, and x-ray tubes, and could be used in the optical range for low-density plasmas. The tremendous development of table-top high-power lasers makes the use of high-intensity, laser-driven K-alpha sources appealing for Talbot–Lau interferometer applications in both high-energy-density plasma experiments and biological imaging. To this end, we present the first, to the best of our knowledge, feasibility study of Talbot–Lau phase-contrast imaging using a high-repetition-rate laser of moderate energy (100 mJ at a repetition rate of 10 Hz) to irradiate a copper backlighter foil. The results from up to 900 laser pulses were integrated to form interferometric images. A constant fringe contrast of 20% is demonstrated over 100 accumulations, while the signal-to-noise ratio continued to increase with the number of shots. Phase retrieval is demonstrated without prior ex-situ phase stepping. Instead, correlation matrices are used to compensate for the displacement between reference acquisition and the probing of a PMMA target rod. The steps for improved measurements with more energetic laser systems are discussed. The final results are in good agreement with the theoretically predicted outcomes, demonstrating the applicability of this diagnostic to a range of laser facilities for use across several disciplines.

https://doi.org/10.1364/AO.398839

1. INTRODUCTION

As the development of high-repetition-rate laser technologies continue to progress and new facilities such as the extreme light infrastructure (ELI) project [1] are built, there is a growing need for reliable diagnostics that are flexible enough to investigate a wide range of experimental conditions. For example, many experiments performed at such facilities rely on photon-absorption diagnostics such as x-ray radiography [2,3]. However, when the subject of investigation is largely transparent to the probing x rays, or if multiple density regimes are being studied, such a technique no longer suffices. Thus, new diagnostics must be developed and deployed at such facilities.

To address this shortcoming in traditional x-ray radiography, several phase-sensitive techniques have been developed [4–6]. By collecting information about the phase of the x rays, these approaches are able to capture refractive effects, observing features such as density gradients without relying on the absorption of x rays. Talbot–Lau interferometry is one such x-ray phase-contrast imaging technique, acting as a grating-based diagnostic, which enables changes to the refractive index of a subject to be observed [4]. This technique has already been established using visible light to probe gaseous flames [7–9] and x rays from synchrotron sources [10] and x-ray tubes [11] and is capable of achieving micrometer-scale spatial resolution. While these x-ray sources make it a valuable diagnostic for use at synchrotron and medical facilities [12], they limit its applicability to laser facilities without readily available coherent x-ray sources. It is therefore desirable to explore and develop other x-ray sources for use in this scheme.

To this end, a proof-of-concept experiment was performed using the high-repetition-rate ECLIPSE laser at the Centre Lasers Intenses et Applications (CELIA) laboratory to irradiate a copper foil, producing K_α radiation at multi-hertz (Hz) frequency. A static PMMA rod was probed using these x rays with a three-grating Talbot–Lau system [13], and multiple pulses were collected to form integrated images. This improved the

final signal-to-noise ratio (SNR) sufficiently so that phase image construction was possible. The SNR was analyzed as a function of photon count, giving a minimum requirement for effective phase-contrast imaging. Using this requirement, an estimation of the minimum pulse energy required for single-shot Talbot–Lau interferometry is calculated.

The remainder of the paper is presented as follows. In Section 2, the theoretical principles behind the design of a Talbot–Lau interferometer are presented. The experimental setup is then described in Section 3. The raw results of this experiment are presented in Section 4 along with a discussion of the signal characteristics. A method for retrieving phase information from the resulting phase-contrast images is described in Section 5 before a final discussion of the reconstructed images, their applicability to high-repetition-rate facilities, and potential optimizations is presented in Section 6. Finally, the paper concludes with a summary of its findings in Section 7.

2. TALBOT–LAU INTERFEROMETER DESIGN THEORY

A Talbot–Lau interferometer relies on a diffractive phenomenon called the Talbot effect. When a plane wave is incident upon a grating, a maximum-contrast image of the grating is repeated at a fixed distance, z_T, given by [14]

$$z_T = \frac{\lambda}{1-\sqrt{1-\frac{\lambda^2}{a^2}}} \approx \frac{2a^2}{\lambda}, \tag{1}$$

where a is the period of the grating, and λ is the wavelength of the incident radiation. The approximation on the right side of this equation assumes that $\lambda \ll a$. Between these points are smaller recreations of this pattern at various distances, forming a "Talbot carpet" [15,16]. Due to the periodic nature of the Talbot carpet, this pattern will continue to repeat at intervals of z_T in planes parallel to the grating. Given a plane of observation a distance R from the grating, it is useful to define the ratio [17]

$$\mu = \frac{1}{z_T}\frac{RR_q}{R+R_q} \approx \frac{R}{z_T}, \tag{2}$$

where R_q is the distance from the source to the grating, and the right-hand approximation assumes $R_q \gg R$. A refined treatment of the wave equation's propagation through such a system shows that a full image of the grating will be reconstructed when $\mu = m/4$, where m is an odd integer known as the Talbot order [17]. The smaller recreations that form the Talbot carpet appear anywhere m is a rational number [18].

Classically, when exposed to an already coherent x-ray source, a Talbot–Lau interferometer can be designed using only two gratings [4]. The first grating, G_1, is placed after the x rays have probed the target and functions as a beam splitter. For this reason, this will be referred to as the "beam-splitter grating" and is responsible for generating the Talbot effect. A second grating, G_2, referred to as the "analyzer grating", is placed at some distance beyond the first. In phase imaging, analyzers are usually used to reject the x rays coming from inelastically or incoherently scattered photons [19]. Its period must be chosen to match the Talbot-recreated pattern at that point in space. It may be shifted laterally to either fully block the pattern or allow it to pass unobstructed. This creates dark- and light-field images, respectively [20]. If, however, there is some small difference between the grating angles, a Moiré pattern will form, alternating between both dark and light fields, allowing the phase to be retrieved without the need for precise lateral alignment [21]. When an object is then placed in the system and perturbs the phase of the x rays, refraction will cause a shift in the Moiré pattern to appear, thereby giving a measurement of the change to the refractive index at that point [21].

Should an x-ray source be incoherent, as is the case in the experiment under consideration here, a "source grating", G_0, may be inserted before G_1. Doing so produces the partial coherence necessary to the first grating to perform diffraction, thereby allowing the Talbot effect to form [20]. Let a_i be the period of grating G_i, and let the distances from the x-ray source to G_0, from G_0 to G_1 and from G_1 to G_2, be denoted by d_s, d_{01}, and d_{12}, respectively. Then, the relationship between a_0 and a_2 is given by [21]

$$\frac{a_0}{a_2} = \frac{d_{01}}{d_{12}}. \tag{3}$$

Under this condition, partial coherence enables the light to interfere constructively and destructively to form the Talbot image. This provides the first constraint in the Talbot–Lau interferometer design.

For the analyzer grating to properly function, it must be in a plane, which has a full Talbot reconstruction of the beam-splitter grating. For any grating, combining Eq. (2) with Eq. (1) and requiring $\mu = m/4$ gives recreated images occurring at

$$R = \frac{m}{2}\frac{a_{\text{eff}}^2}{\lambda}, \tag{4}$$

where a_{eff} is the effective period of the grating in question. The intrinsic phase properties of gratings depend on the phase shift, ϕ, they introduce. This phase shift adjusts the effective period so that [22]

$$a_{\text{eff}} = \frac{a}{\eta}, \tag{5}$$

$$\eta = \begin{cases} 1, & \text{if } \phi = \frac{\pi}{2} \\ 2, & \text{if } \phi = \pi \end{cases}.$$

Note that Eq. (4) only holds for collimated x-ray sources. In the case of diverging sources, the Talbot reconstruction will experience magnification depending on the separation between the gratings. Following the arguments of re-scaling in Fresnel theory [22], in such a system, Eq. (4) must be multiplied by the Talbot magnification, defined as $M_T = 1 + d_{12}/d_{01}$. Then, assigning $R = d_{12}$ and $a = a_1$ to ensure that G_2 is placed at a reconstruction point of G_1,

$$d_{12} = M_T\frac{ma_1^2}{2\eta^2\lambda_0}. \tag{6}$$

This gives the second criterion for designing a Talbot–Lau interferometer.

Finally, Talbot–Lau interferometers are able to accept a degree of polychromatism from their x-ray sources within certain limits

[23,24]. The acceptable bandwidth, $\Delta\lambda$, about the designed wavelength, λ_0, of the system is defined by the grating properties. Should a source be too broadband, z_T will vary too greatly across the source spectrum, and the Talbot reconstruction's contrast will be diminished. To maintain contrast, the source's spectrum must fall within the range of $\lambda_0 \pm \Delta\lambda$, where [24]

$$\Delta\lambda = \frac{\lambda_0}{2m-1}. \tag{7}$$

While the above equations constrain the design of a Talbot–Lau interferometer system, the resulting geometry has the advantage of producing high magnification and fine resolution when probing an object placed between G_0 and G_1 [22].

3. EXPERIMENTAL SETUP

The design of the Talbot–Lau interferometer used in the experiment presented herein is given as follows and presented schematically in Fig. 1. The periods of the source (G_0), beam splitter (G_1), and analyzer (G_2) gratings were, respectively, $a_0 = 2.4$ μm, $a_1 = 3.85$ μm, and $a_2 = 12$ μm. G_0 was a square grating, 2.5 mm × 2.5 mm, while the other two gratings each had 1 cm in diameter circular profiles. These were separated by $d_{01} = 4.67$ cm and $d_{12} = 23.35$ cm, yielding a Talbot order of $m = 3$ and a six times magnification level. G_1 was a π-shift grating, resulting in $\eta = 2$ in Eq. (6).

The backlighter x rays were generated using a high-repetition-rate laser pulse incident on a 100-μm-thick Cu foil, whose normal was angled at 5° to the beam's propagation direction and placed $d_s = 4$ cm from G_0. The laser pulse was 1.5 ps in duration, focused to a 15 μm full-width half-maximum Gaussian spot with 100 mJ of energy in each pulse, giving an intensity of 2.5×10^{16} W cm^{-2} at a wavelength of 810 nm. This produced K_α radiation of 8.05 keV. According to Eq. (7), this gave $\Delta\lambda = 1.6$ keV for an allowable spectrum of 6.4–9.6 keV. To avoid perforation or degradation of the source spectrum, the Cu foil was mounted on a motorized translation stage and translated in-plane between each laser pulse. Additionally, a thin Al foil was placed in front of the source grating (G_0) to protect it from degradation via copper sputtering.

The x rays exiting the Talbot–Lau interferometer setup were filtered using a superposition of 25 μm aluminum, 1 mm polypropylene, and 25 μm beryllium foils. These filters reduced the transmission to approximately 51%. Combined with the 11% transmission of the interferometer itself, the total transmission of the system was therefore reduced to approximately 5.7% ± 0.2% at 8.05 keV. This signal was then collected by a Princeton Instruments 16-bit charge-coupled device (CCD). The CCD had an array of 1340 × 400 pixels with each pixel being 20 × 20 μm in size for a total detector size of 26.8 mm × 8.0 mm, covering approximately a third of the available signal from the interferometer. The combination of filters, system transmission, and camera quantum efficiency allowed x rays with photon energies of 5–15 keV to be detected, easily covering the range required for this experiment. Due to the low photon count, each image captured was the integrated result of 100 backlighter pulses.

The target to be probed was a static PMMA rod, 750 μm in diameter and extending beyond the detector's field of view. Before inserting this target between G_0 and G_1, reference images were taken to obtain a background profile. The target was then inserted, and object images were obtained.

4. DATA ACQUISITION

A. x-Ray Source Spectrum

To obtain a spectrum of the photons reaching the detector, the individual images from the CCD were analyzed given the method given in Ref. [25], which was realized on this very same CCD. This method relies on the fact that the number of photons reaching the detector for each shot was much less than the number of pixels, the photocount approximation could be made. This says that any signal in a given pixel is due to a single photon and, the more energetic the photon, the brighter the signal. The energy deposition of each photon can be made in a single pixel, or it may spread over to its neighbors [25].

Each CCD image was therefore binned by its pixel amplitudes, and the resulting profile was then calibrated using the method described for the CCD given in Ref. [25]. Taking into account the transmission of the system and the quantum efficiency of the CCD camera, the source spectrum was then deduced with a precision of ±5%, as described in Ref. [25], for each pulse.

The obtained spectrum is shown in Fig. 2. As can be seen, the Cu K_α signal dominated the distribution. According to Eq. (7), strong contrast is obtainable, as when the energy falls within the

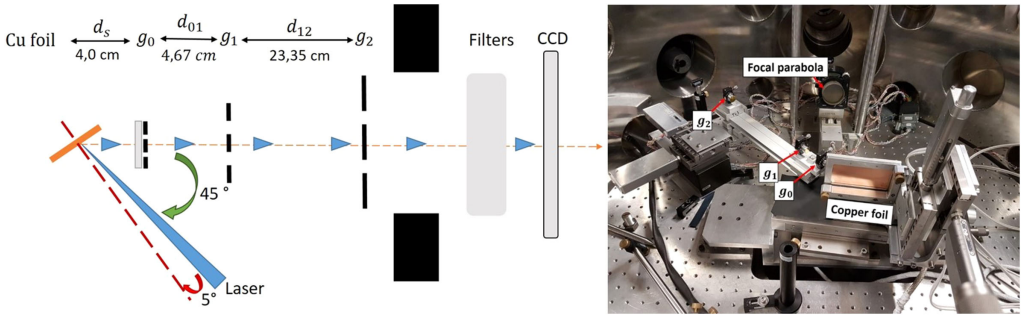

Fig. 1. Schematic of the experimental setup. A laser is focused on a copper foil to produce K_α x-ray emission. The x rays go through G_0 grating to get the spatial coherence necessary at the second grating G_1 to produce a diffraction pattern, which will be filtered by the last grating G_2 before going out of the vacuum chamber and being filtered to avoid saturation before the acquisition on the CCD. On the right image, we can see the experimental setup once in the chamber.

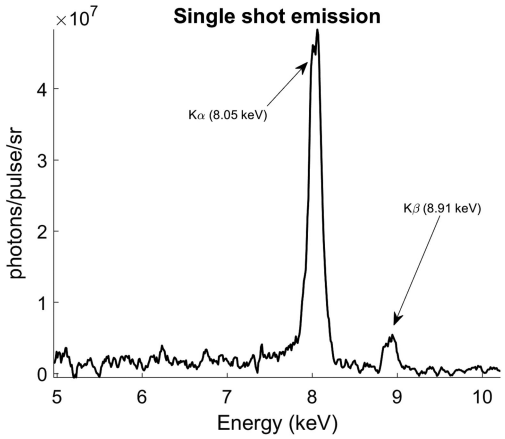

Fig. 2. Estimation of x-ray spectrum retrieved from the emission of a single pulse incident on the copper foil.

8.0 ± 1.6 keV range. Integrating this signal in the acceptable bounds and dividing by the total number of events shows that $75\% \pm 5\%$ of the energy was contained in the desired energy range, indicating that high-quality signals are achievable with this design.

B. Signal Characteristics

High contrast and a strong SNR are required for proper image reconstruction. This subsection analyzes the evolution of the CCD signal's contrast with no target inserted in the system compared to the number of shots integrated into each image.

To calculate these values, multiple signals were added together to form a single integrated image, starting with 100 shots per image and ending with 900 shots per image. Examples of these images are shown in Fig. 3. Note that the perturbations to the signal in the horizontal direction were due to imperfections in the gratings. The SNR was then evaluated from the raw data as

$$\mathrm{SNR} = \frac{\langle I \rangle}{\sigma(I)}, \tag{8}$$

where $\langle I \rangle$ is the local mean intensity of the signal, and $\sigma(I)$ is the local standard deviation of the recorded intensity. To calculate the contrast, a 50-pixel-wide, horizontally integrated, vertical line-out was taken centered at $x = 11$ mm. This width was chosen to reduce the effects of noise on the measured contrast. From this line-out, the maximum and minimum intensities were obtained to calculate the fringe contrast according to

$$C = \frac{I_{\max} - I_{\min}}{I_{\max} + I_{\min}}, \tag{9}$$

where $I_{\max}$ and $I_{\min}$ are the maximum and minimum intensities recorded in CCD for the integrated fringe pattern.

A plot of the contrast and the SNR versus the number of pulses accumulated in each image is shown in Fig. 4. As can be seen in this image, the contrast immediately stabilizes at approximately $22 \pm 2\%$. This is below the ideal case of 30% [26] due to non-ideal gratings, imaging device efficiencies, and source spectrum. However, it is still a large fraction of the ideal

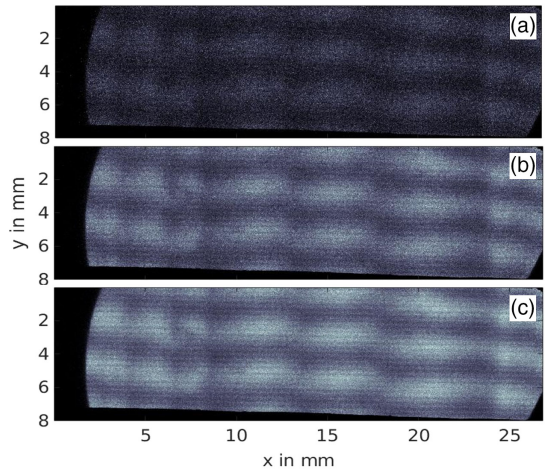

Fig. 3. Evolution of the interference patterns versus the number of laser pulses accumulated: (a) 100 pulses, (b) 500 pulses, (c) 900 pulses.

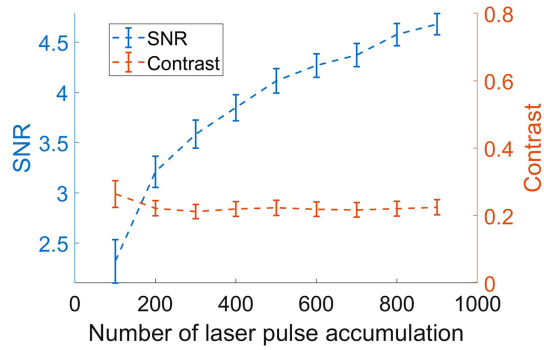

Fig. 4. SNR (blue) and fringe contrast (orange) versus number of laser pulses accumulated.

case and comparable to the 25% achieved with standard setups and x-ray tubes [26], showing that the system is well-designed, and the correct periods and distances have been chosen. It has been shown that optimizations on the x-ray sources can then be performed to reach higher contrast [27], though such improvements were not made here.

Meanwhile, the SNR continues to grow with the number of photons. This demonstrates that the limiting factor in this device's signal acquisition is its photon statistics. This implies that several shots must be integrated together using this x-ray source to properly treat the noise during image processing. The remainder of this paper will focus on the results using 900 shots per image.

5. PHASE RETRIEVAL METHODOLOGY

A. Image Auto-correlation and Noise Reduction

It has been shown previously that enhancing the photon statistics in the acquisition leads to an amelioration of the SNR. It is therefore desirable to integrate multiple sequential images together to improve the photon statistics. However, due to the translation of the Cu foil, it has previously been observed that a slight drift in the fringe patterns will occur between successive

acquisitions. This phenomenon was also observed in previous studies using x-ray tubes [28]. To ensure that the features were properly aligned, the images were correlated together by following a defect in the fringe pattern, which itself was created by grating imperfections.

The noise in the pattern was then processed with an "à trou filter" [29], which preserves the shape of the signal while eliminating outliers. The removal of these outliers is necessary to reduce artefacts in the image reconstruction, which would otherwise introduce nonphysical phase shifts. While not done here, a Wiener filter may also be applied after image retrieval to enhance the results by further reducing noise levels [30].

B. Image Reconstruction

The fringe pattern acquired on CCD can be easily written in complex form as [28,31,32]

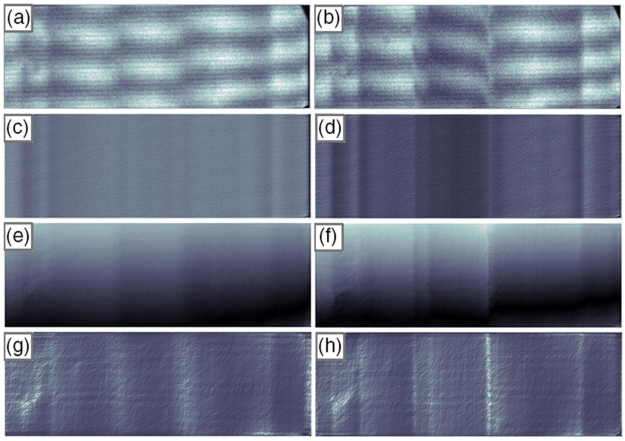

Fig. 5. Separation of variables for the reference (left) and object (right) images. (a), (b) The original signals for the two scenarios were processed to obtain (c), (d) Att images, $A(x, y)$, (e), (f) unwrapped phase images, $\phi(x, y)$, and (g) and (h) DF images, $B(x, y)$.

$$\tilde{I}(x, y) = A(x, y) + B(x, y)e^{i\phi(x,y)}. \tag{10}$$

Here, A, B, and ϕ are all real functions, which relate to the attenuation (Att), dark field (DF), and phase images, respectively [21,32]. To separate these variables, the image is first masked in Fourier space to separate A from the quasi-periodic $Be^{i\phi}$ [32]. To separate B and ϕ from one another, note that $\ln(Be^{i\phi}) = \ln(B) + i\phi$ so that the real part relates solely to B, while the imaginary term corresponds with ϕ.

This process of separating variables was applied to both the reference images and the object images. However, the phase images, $\phi(x, y)$, were originally obtained modulo 2π. Thus, a phase unwrapping algorithm was applied wherein a set of differential equations was solved to directly yield a two-dimensional (2D) unwrapped map [33]. This approach yielded the most robust results, though other techniques such as the geometrical method [31] and least mean square algorithm [34] could be applied as well. The extracted A, B, and unwrapped ϕ images are shown along with the original data in Fig. 5.

Finally, the background signal is removed to obtain the reconstructed Att, DF, and phase difference (Φ) images according to

$$\text{Att} = \frac{A_{\text{obj}}}{A_{\text{ref}}}, \tag{11}$$

$$\text{DF} = \frac{B_{\text{obj}}}{B_{\text{ref}}}, \tag{12}$$

$$\Phi = \phi_{\text{obj}} - \phi_{\text{ref}}, \tag{13}$$

where the subscript "obj" denotes the object image and "ref" the reference image. The results of this final reconstruction are shown in Fig. 6. Profiles were extracted from each of these figures by vertically integrating the entire image and compared to the theoretically predicted transmission and phase shifts. The theoretical phase shift was calculated with the wavefront propagation software, XWFP [35], and the Att profile was estimated using the experimentally measured spectrum and cold opacity for PMMA. As can be seen, the reconstructed data is in fairly

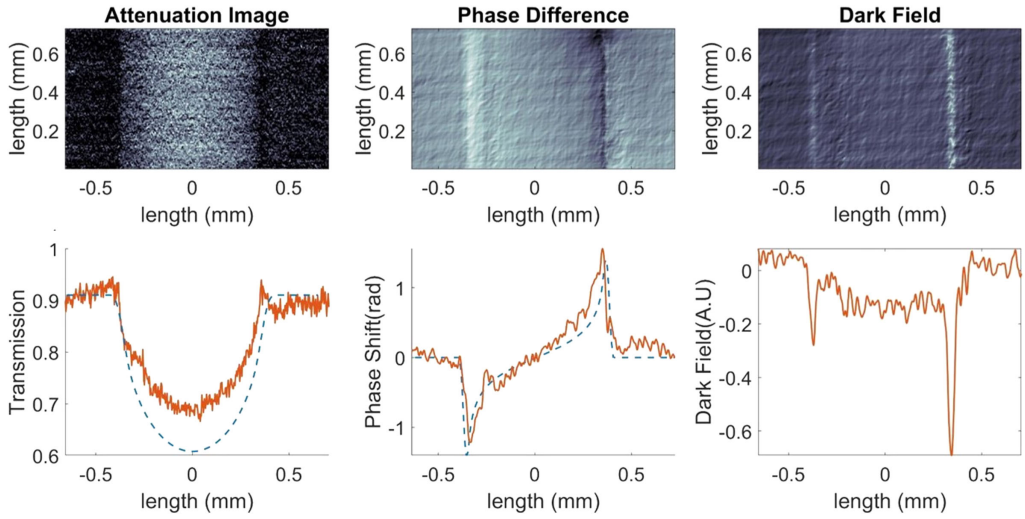

Fig. 6. Reconstructed images (top) are shown and integrated vertically to obtain their one-dimensional profiles (bottom, solid orange) and compared to their theoretically calculated curves (dashed blue). These reconstructed images consist of an absorption radiograph (left), a differential phase-contrast image (center), and a DF image (right).

strong agreement with the predicted profiles. It should be noted that the transmission of the signal outside of the rod was about 90%. This is because the probed images were taken later in the day, and the source grating continued to degrade as shots were accumulated despite the presence of the Al shield. This resulted in debris on the grating and lower overall transmission. To compensate for this effect, the theoretical curve in the transmission image was multiplied by 0.9 to make it directly comparable to the experimentally reconstructed profile.

6. USE FOR HIGH-REPETITION-RATE FACILITIES

A. Resolution of Reconstructed Images

The resolution of each image was measured to be approximately 50 μm ± 5 μm using the sharp boundary at the end of the cylinder. This is consistent with the expected resolution of the system given the source size of 35 μm ± 8 μm. This is of the same order as the theoretically predicted 30 μm resolution for a source size of 40 μm given ideal conditions [26], with the difference likely being due to additional blurring from the CCD, which was not included in the ideal resolution calculation. This demonstrates that the system is well optimized. It should be noted that reducing the source size could improve the resolution to a few microns.

Other experimental modifications can be made to improve the quality of the reconstructed images. For instance, introducing phase stepping techniques is expected to provide vast improvements to the reconstruction quality [21]. This is achieved by laterally shifting the grating positions by a fraction of their period and recording reference images for each configuration. This gives a database of background images that may be used when comparing reference images to probe images [36,37]. Doing so eliminates any phase offsets, which would have otherwise been compensated for through numerical techniques, thereby reducing numerical artefacts and improving the precision of the final results [38,39]. Additionally, while grating degradation was not significant enough to fully degrade our signal, defects became evident at later shots. This required additional correlation of the images together during the analysis of the data. To protect against signal degradation for long accumulation in future experiments, a stronger debris shield should be inserted before G_0 to protect the grating and preserve its structure.

Regardless of these potential improvements, the level of resolution obtained here is already comparable to the resolution of other x-ray imaging diagnostics fielded at high-repetition-rate facilities, such as gated x-ray framing cameras [40], point-source radiography [41], and pinhole imagers [42]. However, because this diagnostic relies on phase-contrast techniques rather than absorption, it is able to observe regimes that would generally be undetectable to standard diagnostics without the large distances required for other phase-contrast diagnostics [6]. This makes it a valuable development for use at laser facilities such as those currently being developed as part of the ELI [43].

B. Single-Shot Imaging Requirements

This paper has demonstrated the ability of this diagnostic to work by aggregating multiple shots together. This is sufficient for probed systems that do not evolve quickly compared to the repetition cycle of the laser. It further suggests that high-repetition-rate lasers could be a promising new x-ray source for such scenarios. However, for systems that evolve much more rapidly, such as high-energy-density plasmas [44–46], single-shot imaging is required. It is therefore interesting to approximate the pulse energy requirements for this to be achieved.

The energy in each pulse used in this experiment was $E_L = 0.1$ J. Integrating the spectrum derived in Section 6. A within the acceptable tolerance of the diagnostic gives an approximate Cu K_α energy of $E_{K\alpha} = (1.3 \pm 0.5) \times 10^{-6}$ J. This gives an overall conversion efficiency ϵ of

$$\epsilon = \frac{E_{K\alpha}}{E_L} = (1.3 \pm 0.5) \times 10^{-5}. \tag{14}$$

This is consistent with other measurements in this intensity regime [47]. The relatively low energy in each pulse meant that the average on-target intensity was approximately 10^{16} W cm^{-2}. However, conversion efficiency increases with intensity. For example, at 10^{19} W cm^{-2}, assuming similar pulse durations and focal spot sizes, the conversion efficiency is expected to increase by a full order of magnitude [47].

To obtain the images presented in this paper, 900 shots were integrated together, implying that 90 J of laser energy was required for each shot. However, larger-scale facilities are able to produce much more intense pulses through tighter focal spots and shorter pulse durations [43]. Indeed, 10^{19} W cm^{-2} intensities are easily achievable at such facilities. As such, due to the higher conversion efficiencies, it is expected that each individual pulse at these higher intensities need only have approximately 10 J of energy to achieve single-shot imaging with this diagnostic. This has already been experimentally observed in Ref. [48].

Smaller systems are capable of taking advantage of this diagnostic through various optimizations. Several systems today are capable of shooting approximately 1 J of energy at 10 Hz [43,49]. With the design used here, images could therefore be produced at approximately 1 Hz, which is already interesting for various applications [47,50,51]. To improve this further, the CCD efficiency must be considered. The imaging device used in the system presented here had a quantum efficiency of approximately 10%. However, devices that do not rely on silicon chips are capable of achieving much greater efficiency in the desired spectrum of around 40% with peak efficiencies of up to 95% at lower x-ray energies. These energies may be achieved by varying the backlighter material, though the grating design would need to be adjusted, and the conversion efficiency reevaluated.

7. SUMMARY

We performed the first Talbot–Lau x-ray imaging at a high-repetition-rate laser facility. Despite some signal degradation due to grating damage, the results from this study show that the diagnostic is stable enough to integrate multiple images

together to improve the SNR. The gratings and distances chosen produced a constant contrast of about 22%, comparable to the theoretical maximum contrast of 30%. This resulted in clear fringe patterns, which were interpreted to form absorption, differential phase, and DF images. The algorithm to do so performed robustly when the noise-to-signal ratio was in excess of four.

Improvements were discussed to further optimize these results including phase stepping methods [36,37] and optimizations of the debris shield before the source grating. Other adjustments to the physical setup, such as x-ray source adjustments and a more efficient imaging device, could provide further enhancements. These adjustments could broaden the applicability of this system to lower-energy facilities. Indeed, several of these steps are already under active investigation [39].

The design presented here has proven to be a robust diagnostic capable of functioning at high-repetition-rate facilities in a more compact space than other x-ray phase-contrast imaging methods [6]. As such, it serves as a powerful tool for exploring new regimes on a broad array of laser systems.

Funding. National Nuclear Security Administration (DENA0002955); Conseil Règional Aquitaine (INTALAX); Agence Nationale de la Recherche (ANR- 10-IDEX-03-02, ANR-15-CE30-0011).

Disclosures. The authors declare no conflicts of interest.

REFERENCES

1. S. Weber, S. Bechet, S. Borneis, L. Brabec, M. Bučka, E. Chacon-Golcher, M. Ciappina, M. DeMarco, A. Fajstavr, K. Falk, E.-R. Garcia, J. Grosz, Y.-J. Gu, J.-C. Hernandez, M. Holec, P. Janečka, M. Jantač, M. Jirka, H. Kadlecova, D. Khikhlukha, O. Klimo, G. Korn, D. Kramer, D. Kumar, T. Lastovička, P. Lutoslawski, L. Morejon, V. Olšovcová, M. Rajdl, O. Renner, B. Rus, S. Singh, M. Šmid, M. Sokol, R. Versaci, R. Vrána, M. Vranic, J. Vyskočil, A. Wolf, and Q. Yu, "P3: an installation for high-energy density plasma physics and ultra-high intensity laser–matter interaction at ELI-beamlines," Matter Radiat. Extremes **2**, 149–176 (2017).
2. J. R. Rygg, O. S. Jones, J. E. Field, M. A. Barrios, L. R. Benedetti, G. W. Collins, D. C. Eder, M. J. Edwards, J. L. Kline, J. J. Kroll, O. L. Landen, T. Ma, A. Pak, J. L. Peterson, K. Raman, R. P. J. Town, and D. K. Bradley, "2D X-ray radiography of imploding capsules at the national ignition facility," Phys. Rev. Lett. **112**, 195001 (2014).
3. F. J. Marshall, P. W. McKenty, J. A. Delettrez, R. Epstein, J. P. Knauer, V. A. Smalyuk, J. A. Frenje, C. K. Li, R. D. Petrasso, F. H. Séguin, and R. C. Mancini, "Plasma-density determination from X-ray radiography of laser-driven spherical implosions," Phys. Rev. Lett. **102**, 185004 (2009).
4. F. Pfeiffer, T. Weitkamp, O. Bunk, and C. David, "Phase retrieval and differential phase-contrast imaging with low-brilliance X-ray sources," Nat. Phys. **2**, 258–261 (2006).
5. F. Pfeiffer, "X-ray ptychography," Nat. Photonics **12**, 9–17 (2018).
6. L. Antonelli, F. Barbato, D. Mancelli, J. Trela, G. Zeraouli, G. Boutoux, P. Neumayer, S. Atzeni, A. Schiavi, L. Volpe, V. Bagnoud, C. Brabetz, B. Zielbauer, P. Bradford, N. Woolsey, B. Borm, and D. Batani, "X-ray phase-contrast imaging for laser-induced shock waves," Europhys. Lett. **125**, 35002 (2019).
7. C. Shakher and A. J. P. Daniel, "Talbot interferometer with circular gratings for the measurement of temperature in axisymmetric gaseous flames," Appl. Opt. **33**, 6068–6072 (1994).
8. M. Thakur, A. Vyas, and C. Shakher, "Measurement of temperature and temperature profile of an axisymmetric gaseous flames using Lau phase interferometer with linear gratings," Opt. Lasers Eng. **36**, 373–380 (2001).
9. M. Thakur, A. L. Vyas, and C. Shakher, "Measurement of temperature profile of a gaseous flame with a Lau phase interferometer that has circular gratings," Appl. Opt. **41**, 654–657 (2002).
10. A. Momose, W. Yashiro, S. Harasse, and H. Kuwabara, "Four-dimensional X-ray phase tomography with Talbot interferometry and white synchrotron radiation: dynamic observation of a living worm," Opt. Express **19**, 8423–8432 (2011).
11. S.-H. Wang, P. O. Margie, M. Atsushi, H. Hua-Jie, R.-F. Hu, Z.-L. Wang, K. Gao, K. Zhang, P.-P. Zhu, and Z.-Y. Wu, "Experimental research on the feature of an X-ray Talbot–Lau interferometer versus tube accelerating voltage," Chin. Phys. B **24**, 068703 (2015).
12. A. Momose, W. Yashiro, K. Kido, J. Kiyohara, C. Makifuchi, T. Ito, S. Nagatsuka, C. Honda, D. Noda, T. Hattori, T. Endo, M. Nagashima, and J. Tanaka, "X-ray phase imaging: from synchrotron to hospital," Philos. Trans. R. Soc. A **372**, 20130023 (2014).
13. M. P. Valdivia, D. Stutman, C. Stoeckl, C. Mileham, I. A. Begishev, W. Theobald, J. Bromage, S. P. Regan, S. R. Klein, G. Muñoz-Cordovez, M. Vescovi, V. Valenzuela-Villaseca, and F. Veloso, "Talbot-Lau x-ray deflectometer electron density diagnostic for laser and pulsed power high energy density plasma experiments (invited)," Rev. Sci. Instrum. **87**, 11D501 (2016).
14. Lord Rayleigh, "XXV. On copying diffraction-gratings, and on some phenomena connected therewith," London Edinburgh Dublin Philos. Mag. J. Sci. **11**(67), 196–205 (1881).
15. W. B. Case, M. Tomandl, S. Deachapunya, and M. Arndt, "Realization of optical carpets in the Talbot and Talbot–Lau configurations," Opt. Express **17**, 20966–20974 (2009).
16. H. F. Talbot, "LXXVI. Facts relating to optical science. No. IV," London Edinburgh Dublin Philos. Mag. J. Sci. **9**(56), 401–407 (1836).
17. J. M. Cowley and A. F. Moodie, "Fourier images IV: the phase grating," Proc. Phys. Soc. London **76**, 378–384 (1960).
18. J. T. Winthrop and C. R. Worthington, "Theory of Fresnel images. I. Plane periodic objects in monochromatic light*," J. Opt. Soc. Am. **55**, 373–381 (1965).
19. D. Paganin, *Coherent X-ray Optics* (Oxford University, 2006).
20. D. Stutman and M. Finkenthal, "Talbot–Lau x-ray interferometry for high energy density plasma diagnostic," Rev. Sci. Instrum. **82**, 113508 (2011).
21. M. P. Valdivia, D. Stutman, C. Stoeckl, C. Mileham, I. A. Begishev, J. Bromage, and S. P. Regan, "Talbot–Lau x-ray deflectometry phase-retrieval methods for electron density diagnostics in high-energy density experiments," Appl. Opt. **57**, 138–145 (2018).
22. T. Donath, M. Chabior, F. Pfeiffer, O. Bunk, E. Reznikova, J. Mohr, E. Hempel, S. Popescu, M. Hoheisel, M. Schuster, J. Baumann, and C. David, "Inverse geometry for grating-based X-ray phase-contrast imaging," J. Appl. Phys. **106**, 054703 (2009).
23. X. Wu, A. Yan, and H. Liu, "A general theory of Talbot–Lau grating interferometry with polychromatic X-ray sources," in *Imaging and Applied Optics 2017 (3D, AIO, COSI, IS, MATH, pcAOP)* (Optical Society of America, 2017), paper MW4C.3.
24. T. Weitkamp, A. Diaz, C. David, F. Pfeiffer, M. Stampanoni, P. Cloetens, and E. Ziegler, "X-ray phase imaging with a grating interferometer," Opt. Express **13**, 6296–6304 (2005).
25. C. Fourment, N. Arazam, C. Bonte, T. Caillaud, D. Descamps, F. Dorchies, M. Harmand, S. Hulin, S. Petit, and J. J. Santos, "Broadband, high dynamics and high resolution charge coupled device-based spectrometer in dynamic mode for multi-keV repetitive X-ray sources," Rev. Sci. Instrum. **80**, 083505 (2009).
26. M. P. Valdivia, D. Stutman, and M. Finkenthal, "Talbot–Lau based Moire deflectometry with non-coherent sources as potential high energy density plasma diagnostic," J. Appl. Phys. **114**, 163302 (2013).
27. J. Rieger, P. Meyer, F. Horn, G. Pelzer, T. Michel, J. Mohr, and G. Anton, "Optimization procedure for a Talbot–Lau x-ray phase-contrast imaging system," J. Instrum. **12**, P04018 (2017).
28. D. Stutman, M. P. Valdivia, and M. Finkenthal, "X-ray Moiré deflectometry using synthetic reference images," Appl. Opt. **54**, 5956–5961 (2015).

29. A. Bijaoui, J.-L. Starck, and F. Murtagh, "Restauration des images multi-echelles par l'algorithme à trous," Traitement du Signal **11**, 229–243 (1994).
30. F. Scholkmann, V. Revol, R. Kaufmann, H. Baronowski, and C. Kottler, "A new method for fusion, denoising and enhancement of X-ray images retrieved from Talbot–Lau grating interferometry," Phys. Med. Biol. **59**, 1425–1440 (2014).
31. M. Takeda, H. Ina, and S. Kobayashi, "Fourier-transform method of fringe-pattern analysis for computer-based topography and interferometry," J. Opt. Soc. Am. **72**, 156–160 (1982).
32. M. Seifert, M. Gallersdorfer, V. Ludwig, M. Schuster, F. Horn, G. Pelzer, J. Rieger, T. Michel, and G. Anton, "Improved reconstruction technique for Moire imaging using an X-ray phase-contrast Talbot–Lau interferometer," J. Imaging **4**, 62 (2018).
33. C. Meneses-Fabian, G. Rodriguez-Zurita, A. Cordero-Davila, and C. Robledo-Sanchez, "Solving differential equations for phase retrieval in Fourier-transform methods," AIP Conf. Proc. **1236**, 118–123 (2010).
34. D. C. Ghiglia and L. A. Romero, "Robust two-dimensional weighted and unweighted phase unwrapping that uses fast transforms and iterative methods," J. Opt. Soc. Am. A **11**, 107–117 (1994).
35. T. Weitkamp, "XWFP: an x-ray wavefront propagation software package for the IDL computer language," Proc. SPIE **5536**, 181–189 (2004).
36. S. Kaeppler, J. Rieger, G. Pelzer, F. Horn, T. Michel, A. Maier, G. Anton, and C. Riess, "Improved reconstruction of phase-stepping data for Talbot–Lau x-ray imaging," J. Med. Imaging **4**, 1–13 (2017).
37. S. Bachche, M. Nonoguchi, K. Kato, M. Kageyama, T. Koike, M. Kuribayashi, and A. Momose, "Laboratory-based x-ray phase-imaging scanner using Talbot-Lau interferometer for non-destructive testing," Sci. Rep. **7**, 6711 (2017).
38. M. P. Valdivia, F. Veloso, D. Stutman, C. Stoeckl, C. Mileham, I. A. Begishev, W. Theobald, M. Vescovi, W. Useche, S. P. Regan, B. Albertazzi, G. Rigon, P. Mabey, T. Michel, S. A. Pikuz, M. Koenig, and A. Casner, "X-ray backlighter requirements for refraction-based electron density diagnostics through Talbot–Lau deflectometry," Rev. Sci. Instrum. **89**, 10G127 (2018).
39. M. P. Valdivia, D. Stutman, C. Stoeckl, C. Mileham, J. Zou, S. Muller, K. Kaiser, C. Sorce, P. A. Keiter, J. R. Fein, M. Trantham, R. P. Drake, and S. P. Regan, "Implementation of a Talbot–Lau x-ray deflectometer diagnostic platform for the OMEGA EP laser," Rev. Sci. Instrum. **91**, 023511 (2020).
40. L. R. Benedetti, J. P. Holder, M. Perkins, C. G. Brown, C. S. Anderson, F. V. Allen, R. B. Petre, D. Hargrove, S. M. Glenn, N. Simanovskaia, D. K. Bradley, and P. Bell, "Advances in x-ray framing cameras at the national ignition facility to improve quantitative precision in x-ray imaging," Rev. Sci. Instrum. **87**, 023511 (2016).
41. R. Tommasini, C. Bailey, D. K. Bradley, M. Bowers, H. Chen, J. M. Di Nicola, P. Di Nicola, G. Gururangan, G. N. Hall, C. M. Hardy, D. Hargrove, M. Hermann, M. Hohenberger, J. P. Holder, W. Hsing, N. Izumi, D. Kalantar, S. Khan, J. Kroll, O. L. Landen, J. Lawson, D. Martinez, N. Masters, J. R. Nafziger, S. R. Nagel, A. Nikroo, J. Okui, D. Palmer, R. Sigurdsson, S. Vonhof, R. J. Wallace, and T. Zobrist, "Short pulse, high resolution, backlighters for point projection high-energy radiography at the national ignition facility," Phys. Plasmas **24**, 053104 (2017).
42. L. R. Benedetti, N. Izumi, S. F. Khan, G. A. Kyrala, O. L. Landen, T. Ma, S. R. Nagel, and A. Pak, "Simplified model of pinhole imaging for quantifying systematic errors in image shape," Appl. Opt. **56**, 8719–8731 (2017).
43. B. Rus, P. Bakule, D. Kramer, J. Naylon, J. Thoma, M. Fibrich, J. T. Green, J. C. Lagron, R. Antipenkov, J. Bartonicek, F. Batysta, R. Base, R. Boge, S. Buck, J. Cupal, M. A. Drouin, M. Ďurák, B. Himmel, T. Havlícek, P. Homer, A. Honsa, M. Horacek, P. Hribek, J. Hubacek, Z. Hubka, G. Kalinchenko, K. Kasl, L. Indra, P. Korous, M. Koselja, L. Koubikova, M. Laub, T. Mazanec, A. Meadows, J. Novak, D. Peceli, J. Polan, D. Snopek, V. Sobr, P. Trojek, B. Tykalewicz, P. Velpula, E. Verhagen, S. Vyhlidka, J. Weiss, C. Haefner, A. Bayramian, S. Betts, A. Erlandson, J. Jarboe, G. Johnson, J. Horner, D. Kim, E. Koh, C. Marshall, D. Mason, E. Sistrunk, D. Smith, T. Spinka, J. Stanley, C. Stolz, T. Suratwala, S. Telford, T. Ditmire, E. Gaul, M. Donovan, C. Frederickson, G. Friedman, D. Hammond, D. Hidinger, G. Cheriaux, A. Jochmann, M. Kepler, C. Malato, M. Martinez, T. Metzger, M. Schultze, P. Mason, K. Ertel, A. Lintern, C. Edwards, C. Hernandez-Gomez, and J. Collier, "ELI-beamlines: progress in development of next generation short-pulse laser systems," Proc. SPIE **10241**, 14–21 (2017).
44. F. Horn, K. Gelse, S. Jabari, C. Hauke, S. Kaeppler, V. Ludwig, P. Meyer, T. Michel, J. Mohr, G. Pelzer, J. Rieger, C. Riess, M. Seifert, and G. Anton, "High-energy x-ray Talbot–Lau radiography of a human knee," Phys. Med. Biol. **62**, 6729–6745 (2017).
45. C. Hauke, P. Bartl, M. Leghissa, L. Ritschl, S. M. Sutter, T. Weber, J. Zeidler, J. Freudenberger, T. Mertelmeier, M. Radicke, T. Michel, G. Anton, F. G. Meinel, A. Baehr, S. Auweter, D. Bondesson, T. Gaass, J. Dinkel, M. Reiser, and K. Hellbach, "A preclinical Talbot–Lau prototype for x-ray dark-field imaging of human-sized objects," Med. Phys. **45**, 2565–2571 (2018).
46. C. Gusenbauer, E. Leiss-Holzinger, S. Senck, K. Mathmann, J. Kastner, S. Hunger, and W. Birkfellner, "Characterization of medical and biological samples with a Talbot–Lau grating interferometer micro XCT in comparison to reference methods," Case Stud. Nondestruct. Test. Eval. **6**, 30–38 (2016).
47. H.-S. Park, D. M. Chambers, H.-K. Chung, R. J. Clarke, R. Eagleton, E. Giraldez, T. Goldsack, R. Heathcote, N. Izumi, M. H. Key, J. A. King, J. A. Koch, O. L. Landen, A. Nikroo, P. K. Patel, D. F. Price, B. A. Remington, H. F. Robey, R. A. Snavely, D. A. Steinman, R. B. Stephens, C. Stoeckl, M. Storm, M. Tabak, W. Theobald, R. P. J. Town, J. E. Wickersham, and B. B. Zhang, "High-energy k-alpha radiography using high-intensity, short-pulse lasers," Phys. Plasmas **13**, 056309 (2006).
48. M. P. Valdivia, D. Stutman, and M. Finkenthal, "Moiré deflectometry using the Talbot–Lau interferometer as refraction diagnostic for high energy density plasmas at energies below 10 keV," Rev. Sci. Instrum. **85**, 073702 (2014).
49. J.-L. Dubois, F. Lubrano-Lavaderci, D. Raffestin, J. Ribolzi, J. Gazave, A. C. L. Fontaine, E. d'Humières, S. Hulin, P. Nicola, A. Poyé, and V. T. Tikhonchuk, "Target charging in short-pulse-laser–plasma experiments," Phys. Rev. E **89**, 013102 (2014).
50. Y. Azamoum, R. Clady, A. Ferré, M. Gambari, O. Utéza, and M. Sentis, "High photon flux kα Mo x-ray source driven by a multi-terawatt femtosecond laser at 100 Hz," Opt. Lett. **43**, 3574–3577 (2018).
51. M. Gambari, R. Clady, A. Stolidi, O. Utéza, M. Sentis, and A. Ferré, "Exploring phase contrast imaging with a laser-based kα x-ray source up to relativistic laser intensity," Sci. Rep. **10**, 6766 (2020).